



## Sub- and supersonic elastic waves in an annular hole phononic metamaterial

Caroline Pouya <sup>1</sup>✉ & Geoff R. Nash <sup>1</sup>✉

Surface acoustic wave (SAW) devices are used in a wide range of applications including sensing and microfluidics, and are now being developed for applications such as quantum computing. As with photonics, and other electromagnetic radiation, metamaterials offer an exciting route to control and manipulate SAW propagation, which could lead to new device concepts and paradigms. In this work we demonstrate that a phononic metamaterial comprising an array of annular hole resonators can be used to realise frequency control of SAW velocity. We show, using simulations and experiment, that metamaterial patterning on a lithium niobate substrate allows control of SAW phase velocities to values slower and faster than the velocity in an unpatterned substrate; namely, to ~85% and ~130% of the unpatterned SAW velocity, respectively. This approach could lead to novel designs for SAW devices, such as delay lines and chirp filters, but could also be applied to other elastic waves.

<sup>1</sup>College of Engineering, Mathematics and Physical Sciences, University of Exeter, Exeter, UK. ✉email: [c.pouya2@exeter.ac.uk](mailto:c.pouya2@exeter.ac.uk); [g.r.nash@exeter.ac.uk](mailto:g.r.nash@exeter.ac.uk)

Surface acoustic waves (SAWs) are elastic waves that travel across the surface of a material and include seismic waves that result in earthquakes over the earth's surface. They can also be generated on the microscale on piezoelectric materials, such as lithium niobate, using interdigital transducers<sup>1</sup> to convert an electrical signal into mechanical motion. SAW devices are used in a range of technologies including SAW filters in the telecommunications industry<sup>2</sup>, SAW sensors<sup>3</sup> and a host of microfluidic applications including atomizers<sup>4,5</sup>, microchannel transport<sup>6</sup>, cell sorting<sup>7</sup>, microfluidic mixing<sup>8</sup> and SAW swimming<sup>9,10</sup>. The outlook for future applications of SAWs with new and improved device functionality is wide-ranging in a variety of acoustics, optics, quantum and microfluidics-based fields with applications from medical diagnostics to quantum computing<sup>11</sup>.

Since the development of the first SAW devices, scientists and engineers have sought to exploit the properties of the different types of SAWs for particular applications. The Rayleigh wave is one important type of SAW and is defined by its elliptical motion comprising predominantly transverse motion (in the vertical plane or 'shear vertical' motion) and longitudinal motion<sup>12</sup>. Another type of SAW is the Love wave, which can be excited with the use of a guiding layer and propagates with transverse motion (in the horizontal plane or 'shear horizontal' motion)<sup>13</sup>. The difference in characteristic motion means that, for example, Love wave devices are attractive for sensing applications in fluids, whereas a Rayleigh wave device in fluid suffers from heaving damping<sup>14</sup>. In addition to a difference in characteristic motion, Love waves also travel with a lower velocity than longitudinal (P) or shear (S) waves, but faster than Rayleigh waves<sup>15</sup>. Rayleigh waves have a frequency-independent velocity, which, for example, is an important attribute for some signal processing applications.

The ability to engineer and control the type of SAW excited in a device, and therefore the characteristic motion and SAW velocity, is highly attractive as it has the potential to allow new devices to be realized with improved performance or functionality and has been the subject of research for the last half century. For example, taking inspiration from electromagnetics, Auld et al.<sup>16</sup> showed that a corrugated surface could be used to allow the propagation of a shear horizontal SAW on a semi-infinite elastic surface, without the need for a guiding layer. Advanced fabrication techniques allow the realization of such gratings for high frequency device operation<sup>14</sup>. One of the most promising ways of controlling SAWs is through the use of phononic crystals (PnCs), which can be engineered to exhibit complete bandgaps (see, for example, refs. 17–20), with a commonly used design being that of etched holes in substrates where bandgaps are defined by the pitch and filling fraction of periodic arrays through Bragg scattering<sup>21,22</sup>. The band structure created by a phononic crystal also allows the SAW group and phase velocity to be altered compared to that within the unpatterned material<sup>23</sup>.

However, the properties of both corrugated surfaces and PnCs are principally determined by their periodicity, and this inherently limits the degrees of freedom available for device design. Arrays consisting of local resonators have been shown to offer greater design freedom as bandgap frequencies and other characteristics are defined not only by the periodicity of the phononic crystal, but also by the properties of the resonators themselves (see, for example, refs. 24–27). In arrays of pillars, coupling between the pillar resonances and SAWs contributes to the formation of a bandgap<sup>28,29</sup> whereas locally resonant annular and spiral holes were also found to induce bandgaps, but with extraordinary extinction ratios<sup>30,31</sup>. Arrays of local resonators have also been used to trap SAWs<sup>32–36</sup>, and even confine propagating SAWs to subwavelength scales<sup>37</sup>.

In this work we demonstrate, through both modelling and experiments, the presence of slow and fast SAWs within an array

of square annular hole resonators, and show that the phase velocity within the array can be controlled via frequency selection. This proof-of-concept demonstration paves the way for further studies of how arrays of local resonators could be used to exploit the characteristics of different types of surface acoustic waves in devices.

## Results and discussion

**Finite element simulations.** Using the finite element modelling software package COMSOL Multiphysics<sup>®38</sup>, the properties of a metamaterial consisting of a square array of square annuli (Array#1 see methods for a complete description of array geometries from COMSOL Multiphysics<sup>®</sup> simulations), patterned onto 128° Y-X lithium niobate, was investigated. Modelled using an eigenfrequency study (Supplementary Fig. 1 shows the eigenfrequency modelled geometry), Fig. 1a shows the calculated band diagram of the square annulus for the first 9 eigenfrequency solutions of the system. The main bandgap region is indicated by grey shading in Fig. 1a and the key frequency of 97 MHz is shown by the magenta dashed line. Figure 1b shows the attenuation (imaginary frequency/real frequency) and Fig. 1c shows the predicted phase velocity determined by calculating  $\frac{\omega}{k}$  from the band diagram in Fig. 1a. The attenuation (Fig. 1b) shows modes that lie below the Rayleigh line (red points) experience less attenuation as expected. Modes above the Rayleigh line (the black points in Fig. 1b) experience more attenuation, but the imaginary component is still much smaller than the real component of frequency. The phase velocity (Fig. 1c) shows that modes below the Rayleigh line (red points) exhibit slower phase velocities as expected from a resonating structure. Modes that are present within the bandgap region lie above the Rayleigh line and exhibit faster velocities (the black points in Fig. 1c), decreasing with increasing frequency.

To model a more realistic array of finite length with a source outside of the array, a frequency domain model (Supplementary Fig. 2 shows the frequency domain modelled geometry from COMSOL Multiphysics<sup>®</sup> simulations) was analysed. The z-displacement fields of SAWs were extracted from cut lines positioned after the designed array at frequencies between 90–130 MHz. The same parameters were extracted from identical positions of an equivalent unpatterned model acting as a reference. From these data, SAW velocities within the resonator array were predicted (see methods and also Supplementary Fig. 3 and 8 for more detail). Average RMS solid displacements were calculated across the same cut line from the patterned and unpatterned models over the analysed frequency range, from which the relative transmission intensity was subsequently calculated. Figure 2 shows the transmission intensity (Fig. 2a) and phase velocities (Fig. 2b) calculated from these models.

The transmission curve (Fig. 2a) shows a reduction in transmission intensity relating to the bandgap induced by the resonator array (Array#1) (see also Fig. 1) and is highlighted by the low transmission region on the graph. Note that, due to the design of the elements within the array, there is still significant transmission of the SAW at some frequencies that lie within the bandgap region (grey), namely in the region of 115–130 MHz. The predicted phase velocity within the array is shown by red and black points in Fig. 2b. The red points indicate predicted slow velocities and the black points show predicted fast velocities. For frequencies that lie in the very low transmission region, the results are not included in Fig. 2b. For frequencies outside the main largest identified bandgap, the SAW propagates with a slower velocity compared to an unpatterned surface. However, for frequencies inside the bandgap region, the SAW propagates faster than that propagating on an unpatterned surface. These

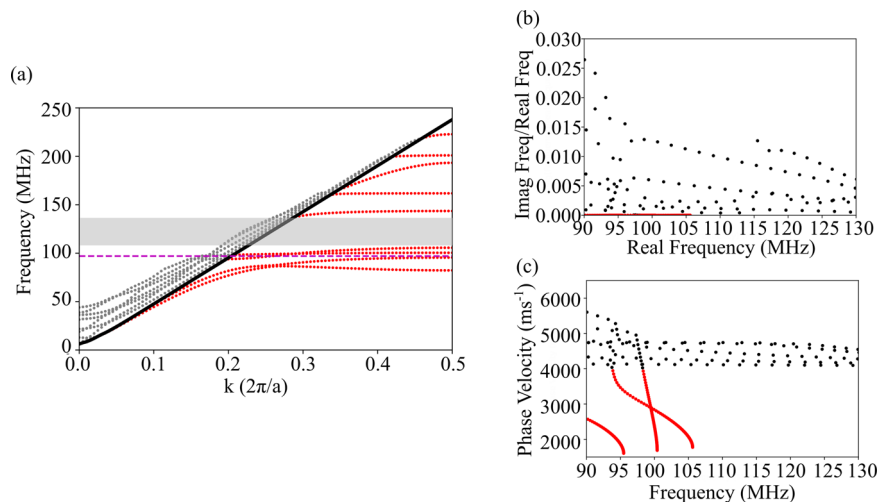


**Fig. 1 Band diagram, attenuation and phase velocity data obtained from Eigenfrequency modelling.** **a** Band diagram of the square annulus used in Array#1. The grey shaded region shows the largest bandgap region and the magenta dashed line is positioned at 97 MHz, i.e. the transducer resonance chosen for characterization. The black line represents the Rayleigh line. Array#1 has a unit cell length  $a=8.4\ \mu\text{m}$ . Grey and red points represent modes above and below the Rayleigh line, respectively. **b** Imaginary frequency divided by real frequency showing attenuation of the system. Black and red points represent modes above and below the Rayleigh line, respectively. **c** Phase velocity of the system calculated from (a). Black and red points represent modes above and below the Rayleigh line, respectively. All plots show the first 9 solutions representing the 9 lowest eigenfrequencies solved in the model for each value of  $k$ . See Supplementary Fig. 4 for data up to solution 12. Data obtained using COMSOL Multiphysics<sup>®38</sup>.

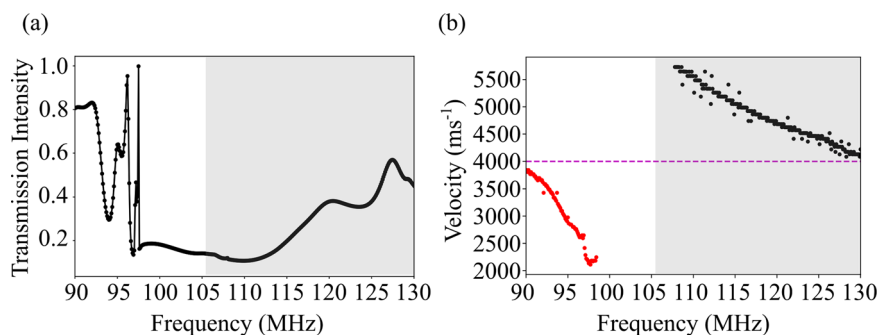


**Fig. 2 Transmission intensity and phase velocity data obtained from frequency domain modelling.** Transmission intensity **a** and calculated phase velocity data **b** obtained from frequency domain models. The patterned model comprises unpatterned areas before and after a patterned array (Array#1) consisting of a  $12 \times 1$  array using periodic boundary conditions for computational efficiency (Supplementary Fig. 2). **a** The black markers highlight the calculated transmitted SAW intensity. **b** Red markers highlight the frequencies predicted to exhibit slower velocities than the standard  $3998\ \text{ms}^{-1}$  and black markers highlight the frequencies predicted to exhibit faster velocities. Grey shaded regions represent the main bandgap region. The magenta dashed line represents the SAW velocity in unpatterned  $128^\circ$  Y-X lithium niobate ( $3998\ \text{ms}^{-1}$ ). Data obtained at 0.1 MHz intervals using COMSOL Multiphysics<sup>®38</sup>.

simulations predict that slow SAWs reach speeds ranging to ~60% of the unpatterned SAW velocity ( $3998\ \text{ms}^{-1}$ <sup>39</sup>), whereas fast SAWs reach speeds ranging to over ~140% of the unpatterned SAW velocity.

The band structure shown in Fig. 1a from 90–130 MHz and the associated allowed eigenmode displacements are related to the frequency dependent transmission, shown in Fig. 2. The differences between Figs. 1c and 2b can be attributed to the nature of the two models. Figure 2 used a finite array with a source outside of the array, and Fig. 1c used an infinite array. Coupling mechanisms and boundary/effects are also likely to alter the wave behaviour depending on the model used. However, Figs. 1c and 2b show strong agreement in phase velocity behaviour and absolute values outside and inside of the main bandgap region. The similar velocity dependence comprises a region of slow velocities that decrease in value with increasing frequency outside of the bandgap and a region of fast velocities inside the bandgap region.

The striking difference in velocities at frequencies inside and outside of the bandgap is further confirmed by examining the

SAW displacements, and Fig. 3 shows simulated out-of-plane ( $z$ ) displacement fields (obtained from model configuration (2) using Array#1 described in the methods section) for frequencies of (a) 90 MHz, (b) 97 MHz, (c) 110 MHz and (d) 120 MHz. The SAW wavefronts outside of the array are clearly visible, and the results qualitatively depict the relative SAW velocity within the array. As shown by the scale bar in Fig. 3, red represents large positive out-of-plane ( $z$ ) displacement fields and blue represents negative out-of-plane ( $z$ ) displacement fields. As expected, the slow SAWs within the array (Fig. 3a, b) are lagging the wavefronts outside of the array, whereas fast SAWs within the array lead the wavefronts outside (Fig. 3c, d). Additionally, the wavelengths within the array appear to shorten or lengthen, consistent with wave theory describing slower and faster velocities, respectively. Note that some non-uniformities seen as local differences in displacements are due to the finite size of the model, and also arise through model meshing tolerances.

For the same fast velocity frequencies analysed in Figs. 3c, d, Figs. 4a, b show deformations (solid displacement and

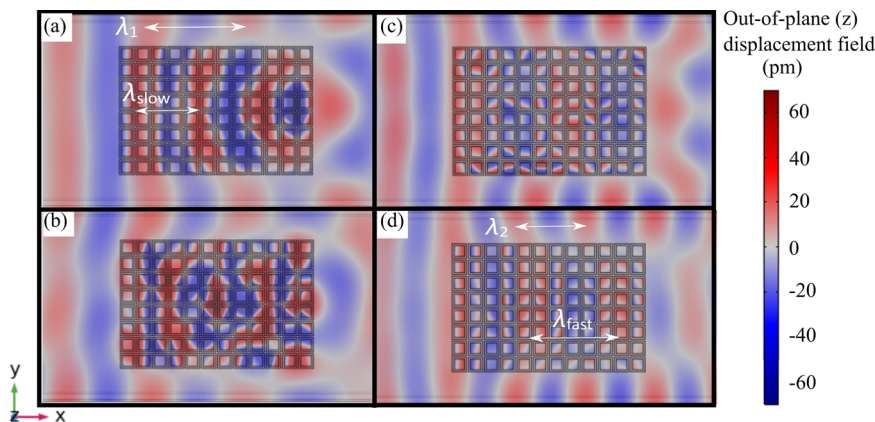


**Fig. 3 Simulated out-of-plane (z) displacement fields.** Simulated out-of-plane (z) displacement fields for (a–b) slow and (c–d) fast phase velocities obtained from model configuration (2). Observed at frequencies of (a) 90 MHz, (b) 97 MHz, (c) 110 MHz and (d) 120 MHz. The wavelength inside the array (Array#1) is shorter and longer than that of the unpatterned surroundings for frequencies that have slow (a–b) and fast (c–d) phase velocities, respectively. Data obtained using COMSOL Multiphysics®<sup>38</sup>.

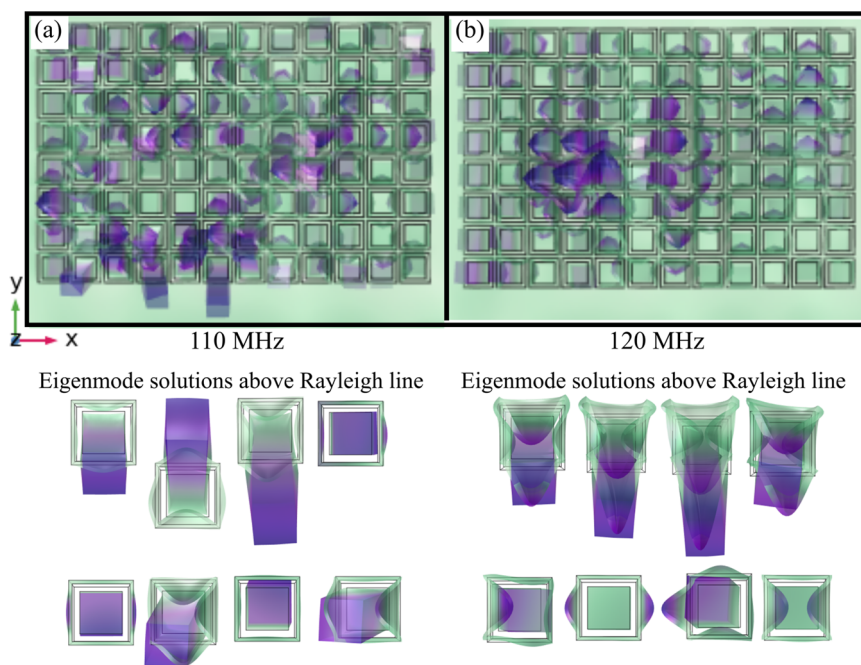


**Fig. 4 Simulated solid displacements with deformations and eigenmodes.** a and b Solid displacements and deformation showing the modes present in the array (Array#1) at 110 and 120 MHz, respectively. Below the main figures are the eigenmodes found above the Rayleigh line up to the first 12 solutions taken from the eigenmode study at or close to the given frequency (see band diagrams Fig. 1 and Supplementary Fig. 4 for higher order modes). Data obtained using COMSOL Multiphysics®<sup>38</sup>.

deformation) of locally resonant modes within the patterned array. Figure 4 shows the deformation data from a finite model at (a) 110 MHz and (b) 120 MHz and below the main figures are the eigenfrequency modes associated with the solutions above the Rayleigh line up to solution 12 obtained from the eigenfrequency analysis modelling and band diagram results (Fig. 1) at the analysed frequencies.

Note, the equivalent band diagram data up to solution 12 are shown in Supplementary Fig. 4. A combination of modes above the Rayleigh line at each frequency can be observed within the finite model array. Therefore the fast velocities can be attributed to a combination of modes existing above the Rayleigh line. As coupling to a variety of the fast modes can be observed in the modes shown in Fig. 4, the velocity is likely to be an average or

combination of those shown for different modes in Fig. 1c at those frequencies.

Figure 4 shows a qualitative depiction of the polarization of modes present in the system within the bandgap region. As can be seen in Fig. 4, at the frequencies in which fast SAWs propagate, there is a change in characteristic motion brought about by displacement polarizations within the array. Namely, there are high amplitude displacements in the y-direction, relating to shear horizontal transverse motion, which is usually small for Rayleigh wave motion. To further investigate the change to Rayleigh wave characteristic motion induced by patterning, the longitudinal, shear horizontal transverse and shear vertical transverse displacement fields within the array, are plotted quantitatively in Supplementary Fig. 5 (see also Supplementary Videos 1, 2 and 3).



The slow SAWs exhibit a Rayleigh-like deformation with substantially increased displacement fields in the transverse vertical direction and the longitudinal direction (Supplementary Fig. 5a, b) with low shear horizontal displacement fields. Propagation is slowed due to the excitation of these strongly resonating elements within the array.

Supplementary Video 1 shows an animation of the Rayleigh motion separated out as components of vertical transverse, horizontal transverse and longitudinal displacement fields in unpatterned lithium niobate and how this relative motion is unchanged by SAW frequency as a comparison. For the patterned array, at frequencies lying in the bandgap region, some transmission is permitted, as shown in Fig. 2a. Supplementary Videos 2 and 3 show an animation of the vertical transverse, horizontal transverse and longitudinal displacement fields in the array and how this relative motion is changed by SAW frequency. For fast SAW frequencies, an increase in horizontal transverse motion and/or longitudinal motion can be observed (Supplementary Videos 2 and 3), for some frequencies this is coupled with a reduction of out-of-plane vertical transverse motion compared with a SAW travelling on unpatterned lithium niobate (Supplementary Video 1). The physical origin of this change in dominant component motion is due to how the deformation of each resonating square element, i.e. the mode shape, changes as a function of frequency.

The square elements have characteristic modes with displacements in a combination of  $x/y/z$  directions which are a result of inherent resonances and eigenmodes of the structure components (Figs. 1 and 4). Ultimately, the polarization of the SAW and the enhancing or reducing of horizontal transverse, vertical transverse and longitudinal motions is determined by the characteristics of the resonating elements and their mode shape at each frequency and therefore may contribute to the differences in phase velocity.

Figure 1 results are from an infinite system with Fig. 2 showing the behaviour in a finite system which more closely represents an experimental system. It is shown in Figs. 1c and 2b that there is a region of slow phase velocities outside of the bandgap region, and a region of fast phase velocities inside of the bandgap region compared to the velocity in unpatterned lithium niobate ( $3998 \text{ ms}^{-1}$ ). The magnitudes of velocities determined by Figs. 1c and 2b agree well for both slow and fast regions. The mechanism of transmission through the finite system within the bandgap region can therefore be inferred from Fig. 1–4 data, as modes existing above the Rayleigh line which can propagate due to low levels of attenuation as shown in Fig. 1b.

**Experimental studies.** Using the results of the modelling, two arrays were designed, fabricated and characterized so that when excited at the same frequency, one exhibits slow propagation, and one fast propagation. The first array (Array#1) had the same geometry as the one discussed above, so that at the excitation frequency used, 97 MHz, the SAW propagated at a slower velocity than in an unpatterned device. In the second array (Array#2), the geometry was adjusted (See methods section ‘Samples’ for dimensions) so that 97 MHz lies within the bandgap region, so that the SAW should propagate at a faster velocity than in an unpatterned device.

Each of the designed arrays were patterned over large areas of lithium niobate devices, between transducers, as shown schematically in Fig. 5a. Focussed ion beam milling was used to pattern the arrays, and Fig. 5c, d, and Fig. 5e, f show electron microscope images of the ‘slow’ and ‘fast’ arrays respectively. The SAWs were imaged using a laser Doppler vibrometer (LDV) which measures the out-of-plane displacements of a defined sample area and

displays the data as a colour map. Figure 6 shows a snapshot of the propagation of SAWs on the patterned (a) ‘slow SAW’ (Array#1) and (b) ‘fast SAW’ (Array#2) devices. Videos showing the propagation from the LDV experiments are shown in Supplementary Videos 4 and 5 for the ‘slow SAW’ (Array#1) and ‘fast SAW’ (Array#2) devices, respectively. An excitation of 97 MHz was used in both cases, corresponding to the resonant frequency of the transducers used. The white dashed lines in Fig. 6 represent the approximate array region within the LDV visible aperture area. LDV measurements were taken within the patterned array and also partly in the unpatterned surroundings. As expected, the slow SAW wavefronts within the patterned area lag the wavefronts in the surrounding, unpatterned area, for the slow SAW device (Array#1) (Fig. 6a). The SAW wavefronts within the patterned area of the fast SAW device (Array#2) lead the wavefronts in the blank surroundings (Fig. 6b). Also apparent is the difference in the wavelength of the SAW within the arrays compared to the surroundings. In the slow array (Fig. 6a) the wavelength has contracted, and in the fast SAW array (Fig. 6b) the wavelength has expanded, consistent with the results obtained from the simulations.

To determine approximate experimental values of the SAW velocity, the wavelengths of the SAWs inside each of the arrays were calculated from the LDV images, using Image J<sup>40</sup>, taking the known wavelength outside of the arrays as a reference. From these measurements, the speed of the SAW in the patterned parts of the slow and fast SAW devices was estimated to be  $0.85v_{\text{SAW}}$  and  $1.31v_{\text{SAW}}$ , respectively, where  $v_{\text{SAW}}$  is the value of the speed of the SAW in unpatterned lithium niobate  $v_{\text{SAW}} = 3998 \text{ ms}^{-1}$ . These are in good agreement with the values of  $0.6v_{\text{SAW}}$  and  $1.35v_{\text{SAW}}$  obtained from the COMSOL Multiphysics® simulations for array #1 and array #2 at 97 MHz, respectively. The difference between the values obtained from the experiments and modelling are likely due to the method of wavelength measurement from the LDV images, namely the resolution of data in Fig. 6 and the estimation of peak-to-peak positions. To reduce this error as much as possible, the slow and fast wavelengths were calculated by averaging i.e. measuring over the largest length containing an integer number of slow/fast wavelengths accessible in Fig. 6 and dividing by the number of wavelengths in that length. Additionally, the geometry of the patterned arrays have some differences to that modelled, due to the limits of the fabrication method, and assumptions made in the model. In particular, the properties of the array are very sensitive to the depths of the holes, and the modelled structures have a square hole region of the annulus whereas the fabricated arrays have more tapered holes (observable in Fig. 5c, e) which will affect the elastic properties of the SAWs and also the transmission and velocity profiles.

Finally, these proof-of-principle results demonstrate the feasibility of creating more complicated arrays to engineer the frequency dependence of the SAW velocity for specific applications. In particular, as the characteristics of the phononic metamaterial are determined in large part by the properties of the individual resonating elements, it should be possible to design an array consisting of resonating elements with tailored geometries to give a SAW velocity that changes continuously as a function of frequency. Ultimately, this approach could be important, for example, for any SAW device that utilize pulses, such as SAW chirp filters, or in the development of new sensors, where each resonator acts as a sensing element. Changes to the environment of a resonator, such as the presence of a gas in the annular hole, would then affect the velocity of the SAW. As common for SAW sensors, this change in velocity would in turn be detected by using the device as a delay line in an oscillator circuit. It may also be beneficial to utilize the different frequency

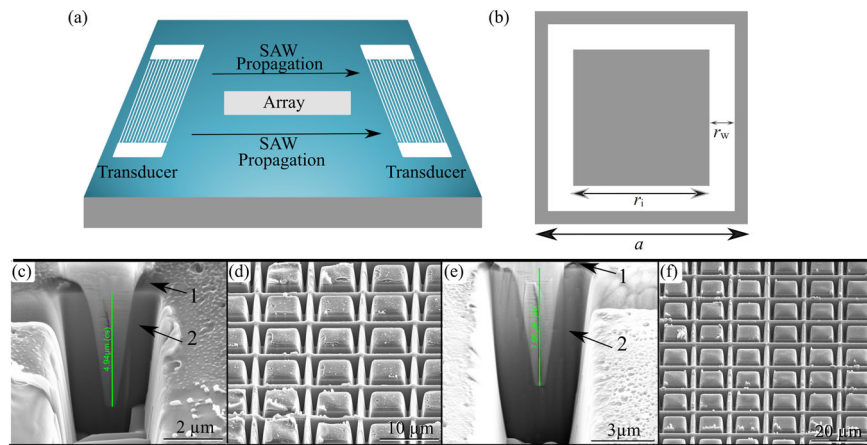


**Fig. 5 SAW device configuration and array pattern geometries.** **a** The lithium niobate device includes the array patterned between the transducers. To excite a SAW, a transducer terminal was connected directly to the LDV source during characterization using SMA cables and connections. Through this connection, a very low voltage was applied with a 97 MHz frequency. Other transducer terminals were connected to a ground plane as appropriate. **b** The unit cell of a square annulus. The grey regions are unmilled lithium niobate and the white region of size  $r_w$  is the area which is focussed ion beam milled to create the annulus. Here  $a$  is the lattice constant,  $r_w$  is the annulus hole width and  $r_i$  is the internal square dimension. Array#1 and Array#2 were designed with different dimensions so the slow and fast SAW regions, respectively, were positioned at 97 MHz. Focussed ion beam milling was used to pattern the square annulus array into lithium niobate chips. Two patterned devices were fabricated and designed to produce **c, d** ‘slow SAWs’ (Array#1) and **e, f** ‘fast SAWs’ (Array#2) at the desired narrowband transducer frequency 97 MHz. Calibrations were obtained outside of the active SAW region to determine the FIB parameters used to create a **c** 4.95  $\mu\text{m}$  and a **e** 7  $\mu\text{m}$  depth annulus for the devices to exhibit slow and fast SAWs, respectively at 97 MHz. The fabricated arrays (**d, f**) were FIB milled into the lithium niobate chips between the two interdigital transducers (**a**). Both comprised  $8 \times 144$  unit cells (with 144 unit cells along the direction of SAW propagation). Label ‘1’ on Fig. c and e shows the PMMA layer and label ‘2’ shows the lithium niobate region.

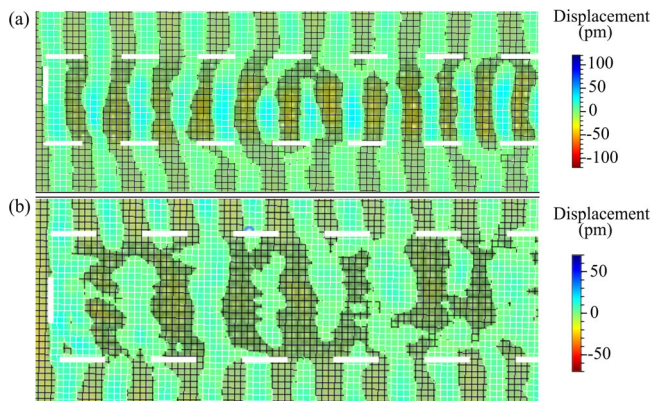


**Fig. 6 Experimental out-of-plane (z) displacement data obtained from LDV measurements.** LDV measurements taken from **a** the ‘slow SAW’ array (Array#1) and **b** the ‘fast SAW’ array (Array#2) at the transducer frequency of 97 MHz. The white dashed lines represent the approximate array region within the analysed LDV aperture area. Measurements were taken within the array and also in the unpatterned surroundings. In the ‘slow SAW’ array **a** SAW wavefronts lag behind the wavefronts in the unpatterned surroundings and in the ‘fast SAW’ array **b** SAW wavefronts lead the wavefronts in the unpatterned surroundings.

regimes with differently polarized modes for sensing of different media, where Rayleigh wave modes have traditionally suffered from heaving damping<sup>14</sup>. However, it should be noted that the geometries presented in this work have not yet been optimized and further work is therefore underway to establish design rules for the realization of arrays optimized for different applications.

## Conclusions

We have demonstrated theoretically and experimentally the presence of slow and fast SAWs in a phononic metamaterial comprising a square lattice of square annuli resonators. The reduction or increase in phase velocity originates from the modes

to which the SAW can couple at a particular frequency and the displacements induced by local resonators within the array. Slow SAWs are achieved as a result of the excitation of the resonators, with greatly enhanced Rayleigh motion, namely vertical transverse and longitudinal motion in the array, slowing the propagation of Rayleigh wave SAWs. Fast SAWs are achieved through coupling to locally resonating propagating modes above the Rayleigh line within the bandgap. We show that due to the allowed modes of the resonators comprising the metamaterial, this velocity change and mode change can be controlled by frequency selection. Our results show 2 distinct regimes; outside the bandgap (slow) or inside the bandgap and above the Rayleigh line (fast) where SAWs at frequencies inside the bandgap are permitted to propagate and transmit through the array. This allows their velocity characteristics to be utilized in applications requiring dynamic velocity control such as wireless sensing and delay line filters. Finally, it is important to note that our metamaterial design has not been optimized for a specific application. However, our results demonstrate the potential of using such a metamaterial design to exploit the characteristics of different types of surface acoustic waves in devices. Our approach could also be scaled to different dimensions and we, therefore, believe that these exciting results will not only be of great interest to researchers in the area of surface acoustic waves, but also to the wider acoustic metamaterial community.

## Methods

**Fabrication.** A commercially available 128 YX-Lithium niobate SAW delay line device, with a centre-to-centre interdigital transducer (IDT) separation distance of 5.4 mm and IDT aperture of 3.25 mm, was used to excite the SAWs. The double-digit IDTs allow the efficient excitation of SAWs at a number of discrete resonant frequencies. We used a FEI Nova 600 dual-beam focussed ion beam/scanning electron microscope to pattern arrays over large areas of lithium niobate devices. Before the lithium niobate could be patterned with the focussed ion beam (FIB) and imaged using the scanning electron microscope (SEM), the sample was coated with a thin layer of metal (gold) to avoid charging. The sample was prepared by spin-coating the lithium niobate with 400 nm of polymethyl methacrylate (PMMA) followed by thermally evaporating a 100 nm layer of gold. PMMA was added before the gold as it can be dissolved with acetone, enabling the gold to be fully removed

before exciting the device with a SAW and taking experimental measurements. The SEM images (Fig. 5) include the layer of PMMA and gold on the surface, but this is not included in the calibration depth measurement of the milled holes (Fig. 5). To calibrate the depth of the array elements, a series of elements were patterned in an area outside of the active SAW region with changing FIB parameters. Platinum was then deposited into the hole region of each element and this area of the element was etched away using the FIB. This exposed the high contrast platinum filled region allowing for a depth measurement to be made (Fig. 5c, e). Once the parameters are calibrated, the array can be patterned. After the array was patterned, the PMMA and gold layers were removed by soaking the sample in acetone. The device was finally mounted on a printed circuit board (PCB) using conductive silver paint and relevant transducer terminals were connected to PCB signal tracks using gold bond wires. PCB signal tracks were connected to SMA connectors to enable cabled connection to experimental equipment for measurements. Other relevant transducer terminals were connected to a ground plane as appropriate.

**Samples.** Two array configurations were fabricated, experimentally characterized and modelled. The unit cell of a square annulus is depicted in Fig. 5b. The grey regions represent unmilled lithium niobate and the white region of size  $r_w$  is the area which was focussed ion beam milled to create the annulus. Array #1 was designed so the slow SAW region was positioned at 97 MHz and had dimensions of lattice constant  $a = 8.4 \mu\text{m}$ , annulus hole depth  $d = 4.95 \mu\text{m}$ , annulus hole width  $r_w = 1 \mu\text{m}$  and the internal square dimension of  $r_i = 5.5 \mu\text{m}$ . Array #2 was designed so the fast SAW region was positioned at 97 MHz and had dimensions of  $a = 11.65 \mu\text{m}$ , annulus hole depth  $d = 7 \mu\text{m}$ , annulus hole width  $r_w = 1.4 \mu\text{m}$  and the internal square dimension of  $r_i = 7.46 \mu\text{m}$ . The equivalent transmission spectrum shown in Fig. 2a for Array #2 is shown in Supplementary Fig. 7 for reference.

**Simulation methods.** The finite element modelling software package COMSOL Multiphysics<sup>®38</sup> was used to determine the displacements and relative transmission intensity of SAWs travelling across arrays patterned onto lithium niobate compared with analogous blank unpatterned lithium niobate. Solid Mechanics and Electrostatics modules were used with Piezoelectric Effect Multiphysics coupling in the frequency domain. The models used an edge load spanning the y-dimension as a 2d line (Supplementary Fig. 2). For computational efficiency two patterned configurations were analysed: a (1)  $12 \times 1$  unit cell array and (2) a  $12 \times 8$  array. The  $12 \times 1$  unit cell array comprised 12 unit cells across the length of the SAW propagation direction (x) with unpatterned regions before and after the array and had periodic boundary conditions (Floquet) covering two sides of the model as shown in Supplementary Fig. 2. The  $12 \times 8$  array had a similar model set-up but had 8 unit cells in the y-direction and was surrounded by a blank unpatterned region on all sides so phase leads and lags within the array could be qualitatively determined with respect to unpatterned areas. Configuration (1), alongside an identical model with no array patterning as the reference, was used to calculate the transmission parameters through the array for each frequency, as plotted in Fig. 2a. A cut line was positioned immediately after the array with a length of several wavelengths. Average RMS solid displacements were calculated across the cut line from the patterned and unpatterned models from which a relative transmission intensity was subsequently calculated (note that the RMS displacement includes the in-plane components, i.e. as  $\frac{1}{\sqrt{2}} \sqrt{A_x^2 + A_y^2 + A_z^2}$ , where  $A_x, A_y,$  and  $A_z$  are the amplitudes in the x,y,z direction, respectively). Model configuration (1) was also used to extract z-displacement field (out-of-plane) data from cut lines after the array (Supplementary Fig. 3) to calculate an estimate of the SAW phase velocity within the finite array. Configuration (1) models were used for data extraction as they had improved mesh and reduced interference from unpatterned regions. Configuration (2) was used alongside to obtain a qualitative visualization of z-displacement field (out-of-plane) data (Fig. 3 and Supplementary Fig. 6 and 8) to estimate the phase position in relation to the unpatterned surrounding area if phase leads or lags were present within the array compared to the unpatterned area and the number/fraction of wavelengths within the array (Supplementary Fig. 8). Configuration 2 was also used to calculate solid displacements and deformations (see Fig. 4).

To calculate the phase velocity from z-displacement field (out-of-plane) data from configuration (1) frequency domain models, both the patterned and unpatterned (reference) models are analysed over identical co-ordinates for each frequency. Therefore the position of a SAW entering the array in the patterned model has the same spatial coordinate and also the same phase as a SAW entering the same region of the unpatterned model for each frequency (position 1). Within the array exists a number of wavelengths,  $n$ , which is not always an integer. Therefore, over the length of the patterned array ( $\text{Length}_{\text{patterned}}$ ),

$$\text{Length}_{\text{patterned}} = n\lambda_{\text{patterned}} \quad (1)$$

where  $n$  is the number or fraction of wavelengths within the length of the array and  $\lambda_{\text{patterned}}$  is the wavelength within the array.

A length measured from position 1 containing the same number/fraction of wavelengths,  $n$ , in the unpatterned reference model for the same excitation frequency,  $\text{Length}_{\text{unpatterned}}$  was determined (see Supplementary Fig. 8 for the depiction of theory description illustrated on a configuration (2) model for demonstrative purposes).

By inspecting z-displacement field (out-of-plane) data of a configuration (2) model the number of  $2\pi$  cycles leading or lagging within the array was identified, and the spatial position at the equivalent point in phase containing  $n$  wavelengths in the unpatterned model was found. Namely, a first guess was made by qualitatively predicting the point in phase containing roughly the same value  $n$  wavelengths in the unpatterned region of configuration (2) model (see Supplementary Fig. 8). To obtain the actual length, the position of the next maximum ( $m1$  in Supplementary Fig. 8) was identified and then  $d1$  was subtracted from  $m1$ , where  $d1$  is a spatial measure of phase calculated from the first peak after the array in the unpatterned transmission region of the patterned model (see Supplementary Fig. 8). Configuration (2) was used to determine the number of  $2\pi$  cycles leading or lagging within the array and Configuration (1) was used to extract data. From the Configuration (1) patterned and unpatterned models, only data after the array was required to find the spatial positions of  $m1$  and the distance  $d1$ , with position 1 already known. From these values, an estimate of  $\text{Length}_{\text{unpatterned}}$  was calculated (see Supplementary Fig. 3 and 8 for further information).

This value is an estimate, as the phase exiting the array is not a smooth sinusoid (see Supplementary Fig. 3). This estimated length  $\text{Length}_{\text{unpatterned}}$  contains the same number or fraction of wavelengths ( $n$ ), i.e.:

$$\text{Length}_{\text{unpatterned}} = n\lambda_{\text{unpatterned}} \quad (2)$$

Using  $f = c/\lambda$

$$f = \frac{c_{\text{Rayleigh}}}{\lambda_{\text{unpatterned}}} \quad (3)$$

$$f = \frac{v_{\text{patterned}}}{\lambda_{\text{patterned}}} \quad (4)$$

where  $c_{\text{Rayleigh}}$  is the speed of SAW propagation in lithium niobate ( $3998 \text{ ms}^{-1}$ ) and  $v_{\text{patterned}}$  is the velocity within the patterned array, which is to be determined. For each analysed frequency, the frequency  $f$  is the same in the patterned and unpatterned system; therefore

$$\frac{c_{\text{Rayleigh}}}{\lambda_{\text{unpatterned}}} = \frac{v_{\text{patterned}}}{\lambda_{\text{patterned}}} \quad (5)$$

Rearranging Eqs. 1 and 2 to make  $\lambda_{\text{patterned}}$  and  $\lambda_{\text{unpatterned}}$  the subject and substituting into Eq. (5) gives

$$\frac{c_{\text{Rayleigh}}^n}{\text{Length}_{\text{unpatterned}}^n} = \frac{v_{\text{patterned}}^n}{\text{Length}_{\text{patterned}}^n} \quad (6)$$

as  $n$  is the same value in each case this can be rewritten as

$$v_{\text{patterned}} = \frac{c_{\text{Rayleigh}} \text{Length}_{\text{patterned}}}{\text{Length}_{\text{unpatterned}}} \quad (7)$$

The process was repeated for each frequency and the calculated phase velocities ( $v_{\text{patterned}}$ ) of each frequency SAW are plotted in Fig. 2b alongside the transmission data.

Configuration (1) was also used with a cut line positioned through the length of the array to measure x, y and z displacement fields in order to investigate longitudinal and horizontal and vertical transverse motions within the array (Supplementary Fig. 5 and Supplementary Videos 2 and 3).

Eigenfrequency models (Supplementary Fig. 1) were used to produce band diagrams showing the eigenmodes of the square annulus (Fig. 1) and to identify the bandgap regions. Floquet boundary conditions were used and surrounded 4 sides of a unit cell of the square annulus (Supplementary Fig. 1). To calculate the Rayleigh line, the same model with no patterning was used. The phase velocity (Fig. 1c) was determined by calculating  $\frac{\omega}{k}$  from the band diagram in Fig. 1a. The attenuation was calculated using imaginary frequency/real frequency calculated directly in eigenfrequency models.

**Laser Doppler vibrometer measurements.** A commercially available Polytec UHF-120 laser Doppler vibrometer (LDV) was used in FFT (frequency) mode to measure the out-of-plane displacements defining the SAW. The device-under-test was affixed to the laser Doppler vibrometer (LDV) stage and securely connected from the LDV frequency source directly to a device transducer terminal using an SMA cable and connections. Through this connection, a very low voltage (1.5 V) was applied to a transducer terminal of the device-under-test at a frequency of 97 MHz (Fig. 5a). A low voltage was used to avoid damaging the transducers. Other transducer terminals were connected to a ground plane as appropriate. A small area of the patterned array was analysed by the LDV under a magnification of 20x and averaged over 3 data sets.

## Data availability

The raw modelling data from Fig. 1 (Supplementary Data 1–4) and to produce Fig. 2 (Supplementary Data 5–7) is provided in the supplementary information accompanying this paper and data analysis methods used to produce Fig. 2 are described throughout this paper. The data used to calculate the simulated Array #2 transmission data shown in Supplementary Fig. 7 is provided in Supplementary data 8 accompanying this paper. The



data used to calculate the simulated phase velocity for Array #2 at 97 MHz is provided in Supplementary data 9–10 accompanying this paper. Original LDV videos from which Fig. 6 was extracted are also provided as Supplementary Videos 4 and 5 accompanying this paper.

Received: 14 July 2020; Accepted: 26 April 2021;

Published online: 03 June 2021

## References

- White, R. M. & Voltmer, F. M. Direct piezoelectric coupling to surface elastic waves. *Appl. Phys. Lett.* **7**, 314 (1965).
- Collins, J. H. & Grant, P. M. The role of surface acoustic wave technology in communication systems. *Ultrasonics* **10**, 59–71 (1972).
- Ballantine, D. S., White, R. M., Martin, S. J., Zellers, E. T., & Wohltjen, H. *Acoustic Wave Sensors* (Academic Press, 1997).
- Kurosawa, M., Watanabe, T., Futami, A. & Higuchi, T. Surface acoustic wave atomizer. *Sens. Actuators A* **50**, 69–74 (1995).
- Chono, K., Shimizu, N., Matsui, Y., Kondoh, J. & Shiokawa, S. Development of novel atomization system based on SAW streaming. *J. Appl. Phys.* **43**, 2987 (2004).
- Cecchini, M., Girardo, S., Pisignano, D., Cingolani, R. & Beltram, F. Acoustic-counterflow microfluidics by surface acoustic waves. *Appl. Phys. Lett.* **92**, 104103 (2008).
- Franke, T., Braunmüller, S., Schmid, L., Wixforth, A. & Weitz, D. A. Surface acoustic wave actuated cell sorting. *Lab. Chip* **10**, 789–794 (2010).
- Frommelt, T. et al. Microfluidic mixing via acoustically driven chaotic advection. *Phys. Rev. Lett.* **100**, 034502 (2008).
- Bourquin, Y. & Cooper, J. M. Swimming using surface acoustic waves. *PLoS ONE* **8**, e0042686 (2013).
- Pouya, C., et al Frequency dependence of surface acoustic wave swimming. *J. R. Soc. Interface* **16**, 20190113 (2019).
- Delsing, P. et al. The 2019 surface acoustic waves roadmap. *J. Phys. D Appl. Phys.* **52**, 353001 (2019).
- Lord Rayleigh. On waves propagated along the s-plane of an elastic solid. *Proc. London Math. Soc.* **17**, 4–11 (1885).
- Love, A. E. H. *Some Problems of Geodynamics* 89–104, 149–152 (UK Cambridge University Press, 1911).
- Xu, J., Thakur, J. S., Zhong, F., Ying, H. & Auner, G. W. Propagation of a shear-horizontal surface acoustic mode in a periodically grooved AlN/Al<sub>2</sub>O<sub>3</sub> microstructure. *J. Appl. Phys.* **96**, 212 (2004).
- Soomro, R. A., Weidle, C., Cristiano, L., Lebedev, S. & Meier, T., PASSEQ Working Group. Phase velocities of Rayleigh and love waves in central and northern Europe from automated, broad-band, interstation measurements. *Geophys. J. Int.* **204**, 517–534 (2016).
- Auld, B. A. & Gagnepain, J. J. Horizontal shear surface waves on corrugated surfaces. *Electron. Lett.* **12**, 650–651 (1976).
- Cheng, W., Wang, J., Jonas, U., Fytas, G. & Stefanou, N. Observation and tuning of hypersonic bandgaps in colloidal crystals. *Nat. Mater.* **5**, 830–836 (2006).
- Wang, Y. F., Wang, Y. S. & Su, X. X. Large bandgaps of two-dimensional phononic crystals with cross-like holes. *J. Appl. Phys.* **110**, 113520 (2011).
- Pourabolghasem, R., Mohammadi, S., Eftekhari, A. A., Khelif, A. & Adibi, A. Experimental evidence of high-frequency complete elastic bandgap in pillar-based phononic slabs. *Appl. Phys. Lett.* **105**, 231908 (2014).
- Kulpe, J. A., Sabra, K. G. & Leamy, M. J. Acoustic scattering from phononic crystals with complex geometry. *J. Acoust. Soc. Am.* **139**, 3009–3020 (2016).
- Benchabane, S. et al. Observation of surface-guided waves in holey hypersonic phononic crystal. *Appl. Phys. Lett.* **98**, 171908–171908–3 (2011).
- Zhu, R., Liu, X. N., Hu, G. K., Sun, C. T. & Huang, G. L. Negative refraction of elastic waves at the deep-subwavelength scale in a single-phase metamaterial. *Nat. Commun.* **5**, 5510 (2014).
- Deymier, P. A. *Acoustic Metamaterials and Phononic Crystals*, Springer-Verlag Berlin Heidelberg. Part of the Springer Series in Solid-State Sciences book series (SSSOL, volume 173) 2013.
- Pennec, Y., Djafari-Rouhani, B., Larabi, H., Vasseur, J. O. & Hladky-Hennion, A. C. Low-frequency gaps in a phononic crystal constituted of cylindrical dots deposited on a thin homogeneous plate. *Phys. Rev. B* **78**, 104105 (2008).
- Wu, T. T., Huang, Z. G., Tsai, T. C. & Wu, T. C. Evidence of complete band gap and resonances in a plate with periodic stubbed surface. *Appl. Phys. Lett.* **93**, 11902 (2008).
- Colquitt, D. J., Colombi, A., Craster, R. V., Roux, P. & Guenneau, S. R. L. Seismic metasurfaces: sub-wavelength resonators and Rayleigh wave interaction. *J. Mech. Phys. Sol.* **99**, 379–393 (2017).
- Raguin, L. et al. Dipole states and coherent interaction in surface-acoustic-wave coupled phononic resonators. *Nat. Commun.* **10**, 4583 (2019).
- Khelif, A., Achaoui, Y., Benchabane, S., Laude, V. & Aoubiza, B. Locally resonant surface acoustic wave band gaps in a two-dimensional phononic crystal of pillars on a surface. *Phys. Rev. B Condens. Matter Mater. Phys.* **81**, 21403 (2010).
- Achaoui, Y., Laude, V., Benchabane, S. & Khelif, A. Local resonances in phononic crystals and in random arrangements of pillars on a surface. *J. Appl. Phys.* **114**, 104503 (2013).
- Ash, B. J., Worsfold, S. R., Vukusic, P. & Nash, G. R. A highly attenuating and frequency tailorable annular hole phononic crystal for surface acoustic waves. *Nat. Commun.* **8**, 174 (2017).
- Kyrimi, V., Ash, B. J. & Nash, G. R. A metasurface comprising spiral shaped local resonators for surface acoustic waves. *J. Phys. D Appl. Phys.* **52**, 345306 (2019).
- Laude, V., Robert, L., Daniau, W., Khelif, A. & Ballandras, S. Surface acoustic wave trapping in a periodic array of mechanical resonators. *Appl. Phys. Lett.* **89**, 083515 (2006).
- Colombi, A., Colquitt, D., Roux, P., Guenneau, S. & Craster, R. V. A seismic metamaterial: the resonant metawedge. *Sci. Rep.* **6**, 27717 (2016).
- Benchabane, S. et al. Surface-wave coupling to single phononic subwavelength resonators. *Phys. Rev. Appl.* **8**, 034016 (2017).
- Chaplain, G. J., De Ponti, J. M., Aguzzi, A., Colombi, A. & Craster, R. V. Topological rainbow trapping for elastic energy harvesting in graded Su-Schrieffer-Heeger systems. *Phys. Rev. Appl.* **14**, 054035 (2020).
- De Ponti, J. M. et al. Graded elastic metasurface for enhanced energy harvesting. *New J. Phys.* **22**, 013013 (2020).
- Ash, B. J., Rezk, A. R., Yeo, L. Y. & Nash, G. R. Subwavelength confinement of propagating surface acoustic waves. *Appl. Phys. Lett.* **118**, 013502 (2021).
- COMSOL Multiphysics® v. 5.5 and v 5.6. <https://www.comsol.com> (COMSOL AB) (2019, 2020).
- Slobodnik, A. J. & Conway, E. D. Microwave Acoustics Handbook Vol 1. Surface Wave Velocities. *J. Acoust. Soc.* **56**, 1307 (1974).
- Rasband, W. S., ImageJ, U.S. National Institutes of Health, Bethesda, Maryland, USA. <https://imagej.nih.gov/ij/> (1997–2018).

## Acknowledgements

The authors would like to thank Dr B. J. Ash, Dr P. V. Dakappa, Dr H. Chang, and Dr M. Heath from the University of Exeter for helpful discussions and technical assistance. This work was funded by a Leverhulme Trust Research Project Grant, number RPG-2017-60.

## Author contributions

G.R.N. conceived the study and guided the experiments and theoretical modelling; C.P. fabricated samples, performed experiments and performed the theoretical analysis; C.P. and G.R.N. wrote the manuscript.

## Competing interests

The authors declare no competing interests.

## Additional information


**Supplementary information** The online version contains supplementary material available at <https://doi.org/10.1038/s43246-021-00163-w>.

**Correspondence** and requests for materials should be addressed to C.P. or G.R.N.

**Peer review information** Primary handling editor: Aldo Isidori

**Reprints and permission information** is available at <http://www.nature.com/reprints>

**Publisher's note** Springer Nature remains neutral with regard to jurisdictional claims in published maps and institutional affiliations.

 **Open Access** This article is licensed under a Creative Commons Attribution 4.0 International License, which permits use, sharing, adaptation, distribution and reproduction in any medium or format, as long as you give appropriate credit to the original author(s) and the source, provide a link to the Creative Commons license, and indicate if changes were made. The images or other third party material in this article are included in the article's Creative Commons license, unless indicated otherwise in a credit line to the material. If material is not included in the article's Creative Commons license and your intended use is not permitted by statutory regulation or exceeds the permitted use, you will need to obtain permission directly from the copyright holder. To view a copy of this license, visit <http://creativecommons.org/licenses/by/4.0/>.

© The Author(s) 2021